Aerodynamic Variables and Loads Estimation Using Bio-Inspired Distributed Sensing

Sergio A. Araujo-Estrada*, and Shane P. Windsor†
Department of Aerospace Engineering, University of Bristol, UK

Conventional control systems for autonomous aircraft use a small number of precise sensors encoding centre of mass motion and generally are setup for flight regimes where rigid body assumptions and linear flight dynamics models are valid. Flying animals in contrast take advantage of highly non-linear structural dynamics and aerodynamics to achieve efficient and robust flight control. It appears that the distributed arrays of flow and force sensors found in flying animals play a key roll in enabling their remarkable flight control. This paper presents current research using a wing model instrumented with distributed arrays of load and flow sensors to provide estimates of a range of aerodynamic and load related variables. The characteristics of instrumentation on the wing model, as well as those of a 1-DOF pitch rig are described and characterisation experiments carried out in a closed circuit low turbulence wind tunnel are presented. The results from these experiments show that a wealth of information can be extracted from the pressure and strain signals, including the state of the flow around the wing, and rate dependent non-linear structural and aerodynamic behaviour over a wide range of angles of attack, including well into the stall region. Using the signals from the distributed array Artificial Neural Networks were trained to provide estimates of angle of attack, airspeed, drag, lift and pitching moment. The networks were able to accurately estimate α (RMS error $0.15°$), airspeed (RMS error $0.15\,\mathrm{m/s}$ – 1.25% Full-Scale-Error (FSE)), drag (RMS error $0.33\,\mathrm{N}$ – 1.78%FSE), lift (RMS error $0.57\,\mathrm{N}$ – 0.60%FSE) and pitching moment (RMS error $0.03\,\mathrm{N\,m}$ – 5.00%FSE). These estimators provided good estimates even in the stall region when the distributed array pressure and strain signals became unsteady. Future applications based on distributed sensing could include enhanced flight control systems that directly use measurements of aerodynamic states and loads, allowing for increase manoeuvrability and improved control of UAVs with high degrees of freedom such as highly flexible or morphing wings.

Nomenclature

Roman Symbols

D	Aerodynamic drag force, N
L	Aerodynamic lift force, N
M	Aerodynamic pitching moment, N m
c	Wing model mean aerodynamic chord, m
q	Wing model pitch rate, °/s
b	Wing model span, m
S	Wing model reference surface, m^2
V	Wind speed, m/s

Greek Symbols

*Research Associate, s.araujoestrada@bristol.ac.uk.
†Lecturer in Aerodynamics.

α Angle of attack, $^\circ$

ρ Air density, kg/m^3

I. Introduction

Conventional flight control systems for autonomous aircraft traditionally utilise a small number of very precise sensors which give the control system information about the motion of the aircraft's centre of mass. For instance, inertial measurement units (IMUs) are used to measure linear acceleration and angular rates of rotation, while a single pitot tube measures airspeed. This information is then normally used alongside sensors such as GPS to provide the control system with measurements of the aircraft rigid body motion [1]. This conventional range of sensor input works well when the assumptions of rigid body motion and linearised flight dynamics and aerodynamics apply, but may be limiting when these assumptions are no longer valid; for example, with highly flexible airframes or at high angles of attack. In these cases, the dynamics involved can become highly non-linear and conventional sensors suites may not be sufficient to characterise the dynamic state of the aircraft.

Biological flyers such as birds, bats and insects all have highly flexible wings and bodies, where numerous joints and aeroelastic deformation means that the shape of their wings and the related aerodynamic forces they produce is constantly changing [2]. In addition, they fly in airflows where the magnitude of gusts can be the same order as their airspeed, meaning that they can experience very large unpredictable changes in angle of attack [3]. Rather than being limited by these departures from rigid body motion and liner aerodynamics it appears that biological flyers take advantage of these. For instance, wing flexibility helps reduce the flight costs of locusts [4], flapping motion generates additional lift through leading edge vortex generation in bats [5], and birds appear to use both spatial [6] and temporal variation [7] in the wind to reduce their flight costs.

One aspect all biological flyers appear to have in common, and in contrast to aircraft, is that they have many different sensors distributed on their bodies and aerodynamic surfaces, as well as having localised sensory organs such as eyes, ears and inertial sensors. Insects have many flow sensitive hairs distributed about their bodies, as well as strain sensitive campaniform sensile distributed throughout their wings [8]. Birds have thousands of mechanoreceptors throughout their wings [9] which are thought to encode airflow information [10], while also having proprioceptive muscle spindles which give them information about the positions of the different parts of their body and the forces acting on these [11]. Similarly, bats have flow sensitive hairs distributed over their wings [12], as well as very similar proprioceptive organs to birds. Overall, these types of distributed sensors provide animals with a rich suite of sensory input about the spatial distribution of airflow and loading over their bodies and wings and it would appear that these distributed sensory systems play an important role in their robust and efficient flight control.

The development of distributed airflow sensor systems is a growing research area. Distributed flow sensors have been used in Flush Air Data Aystems (FADS) in a number of high performance aircraft, such as the X-33 [13] and the space shuttle [14], where traditional airdata booms were impractical. However, these distributed airflow sensors are also increasingly being developed for small unmanned air vehicles (UAVs) where there is a need for more agile flight control when flying in cluttered turbulent environments. These systems have utilized a number of different types of sensors such as diaphram based pressure sensors [15], hot film sensors [16] and artificial hair sensors [17]. Studies of these systems in wind tunnel testing, as well as flight testing [18], have shown the potential of these systems for measuring a range of aerodynamic parameters.

The use of distributed force or strain measurement for flight control is a less well investigated area than distributed flow sensing. Initial work has shown the potential for this type of sensor information to improve flight control, with the potential for faster responses [19] and the use of a physics based control approach [20]. Previous studies have looked at the advantages of each system in isolation in separate aircraft [21], but as yet the potential advantages of utilizing both distributed airflow and load information in a single aircraft have not been well explored.

This paper presents results of ongoing research investigating the potential application of bio-inspired distributed sensing to estimate aerodynamic variables and loads in small scale fixed wing UAVs. This paper is organised as follows: Section II presents the experimental methods and platforms used for this research and their main characteristics. Section III presents results from wind tunnel tests carried out to characterise the strain and pressure signals. Section IV presents aerodynamic variables and loads prediction results using strain and pressure experimental data. Section V summarises the information presented in this paper, and discusses areas of potential application for distributed sensing.

II. Experimental Platform Description

A. Wing model

A wind tunnel wing model with a distributed array of sensors was designed and integrated. The wind tunnel model was constructed using the main wing of a radio control aircraft model (Ripmax, Wot4 Foam-E Mk2+). The wing is of rectangular shape, with a wingspan of $b = 1.205$ m and a chord of $c = 0.25$ m (note that the mean aerodynamic chord is equal to the chord). Only half of the wing was used for the model, i.e. the wind tunnel model wingspan is 0.602 m. The sensing array was composed of pressure and strain sensors. A total of 30 pressure sensors were connected to corresponding pressure ports. They were distributed along the wing chord and installed in two different locations along the span using 3D-printed inserts. The chord-wise location of the pressure ports is shown in Figure 2a, while the span-wise location of the 3-D inserts is shown in Figure 2b. This arrangement provided information on the chord-wise pressure distribution of the wing at two locations along the span. An array of 16 strain gauges was installed on an aluminium beam located at the quarter chord of the wing. The strain gauges were divided into four sub-arrays, with each sub-array able to measure vertical bending and torsional moments. Figure 2b shows the span-wise location of each strain gauge sub-array. The sensor technical specifications are given in Table 1. Higher range pressure sensors were used in parallel with lower range sensors for some ports where there was potential for the sensors to saturate, with their signals fused in the data processing stage. The wing model was fitted with two servo motors to drive the motion of the wing control surfaces. A pitot tube was installed on the wing to provide auxiliary airspeed readings. Figure 1 shows a picture of the wing model experimental platform distributed sensing array layout and the model when installed in the wind tunnel.

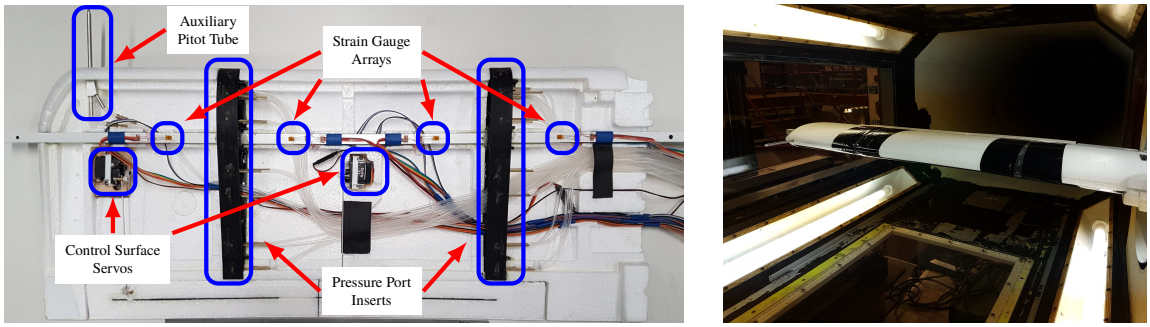

(a) (b)

Figure 1 Wing model experimental platform: (a) distributed sensing array on wing and (b) model installed in wind tunnel.

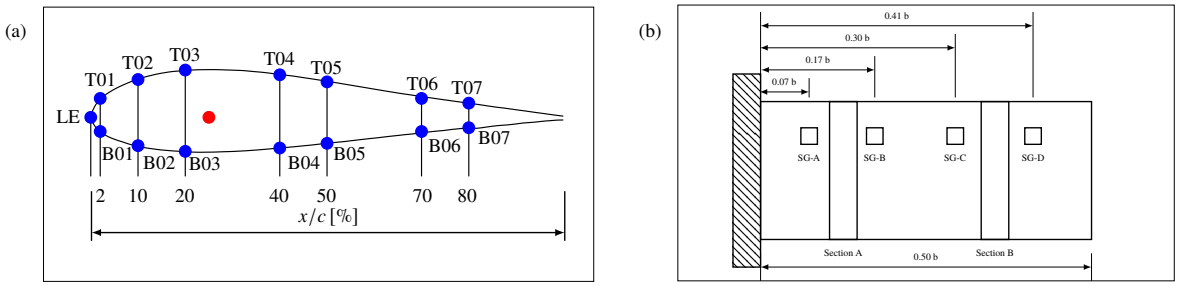

Figure 2 Wing model experimental platform sensor locations: (a) chord-wise pressure array distribution and (b) span-wise strain array distribution.

Table 1 Wing model experimental platform sensor technical specifications.

Feature	Sensors			
Measurement	Static pressure	Static pressure	Vertical bending	Torsion
Model	SDP36	MPXV7002	SGD-2/350-DY11	SGD-2/350-RY51
Manufacturer	Sensirion	Freescale Semiconductor	Omega Engineering	Omega Engineering
Measurement range	±500 Pa	±2 kPa	-	-

B. 1-DOF pitch rig

The wing model was mounted on a 1-Degree-Of-Freedom (DOF) pitch motion wind tunnel rig, with the motion driven by a servo motor (Schneider Electric, LXM32MD30M2). Figure 3a shows a schematic representation of the 1-DOF pitch motion wind tunnel rig layout. The aerodynamic loads were measured using a load cell (ATI, Mini 45) mounted at the interface between the wing support and the rig's shaft. A timing pulley-belt array connected on one end to the rig's shaft and on the other to a magnetic rotary encoder (Renishaw, RMB20SC). This sensor provided measurements of the angle of attack. The rig's shaft was connected to the servo motor through a elastomer insert coupling (R+W, EKH-60-B-24-28).

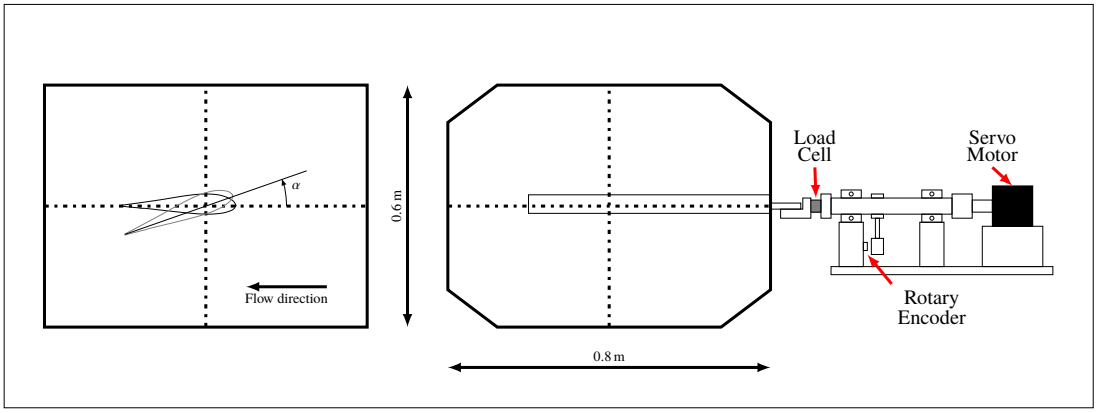

(a)

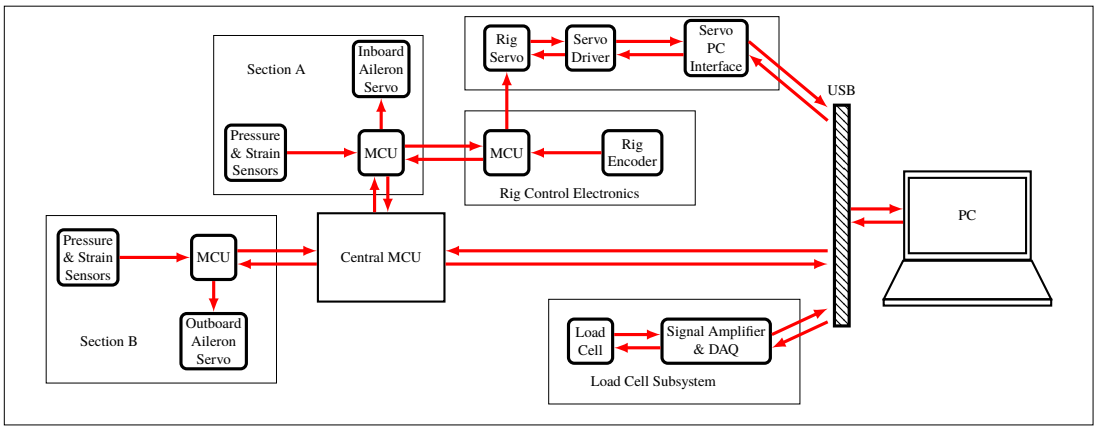

(b)

Figure 3 Pressure & strain sensing experimental platform: (a) wind tunnel layout and (b) DAQ system.

C. Data acquisition system

A custom data acquisition (DAQ) system, including some proprietary hardware, was used to collect pressure, strain, aerodynamic loads and aerodynamic variables data. Figure 3b shows a block diagram of the DAQ system. The DAQ system was divided into seven Micro-Controller Unit (MCU) based subsystems: the Section A subsystem acquired the signals from the pressure sensors in Section A insert and the SG-A and SG-B strain gauge arrays, it received and stored data from the rig control electronics and controls the inboard servo motor; the Section B subsystem acquired the signals from the pressure sensors in Section B insert and the SG-B and SG-C strain gauge arrays and controlled the outboard servo motor; the rig control electronics subsystem acquired the angle of attack rig encoder signal and was used as an alternative system to control the motion of the rig's servo; the central MCU subsystem received time stamped data acquired by Section A, Section B and rig control electronics subsystems and transmitted it to a PC via USB communication. This subsystem can also be used to transmit commands generated by the PC to the other subsystems. The load cell subsystem measured, acquired, conditioned and transmitted load signals to a PC via USB using a multi-function I/O device (NI, USB-6218); the rig servo subsystem controlled the motion of the servo. Lastly the PC collected and stored pressure, strain, aerodynamic loads and aerodynamic variables data. The servo motor motion commands can be generated by the PC using Schneider Electric SoMove software or by the rig control electronics MCU, which allows for automatically generated inputs or tracking of an external analogue signal.

All acquired data was sampled at 200 Hz by the appropriate subsystem and received by the PC. It was then routed using User Datagram Protocol (UDP) messages and stored on disk by a custom graphical user interface (GUI) written in Python. A Simple Network Time Protocol (SNTP) was used to synchronise the clock signal of the MCU subsystems with the PC clock signal. The SNTP implementation achieves a maximum time offset of less than 1.0 ms between clock signals. Results from a series of characterisation experiments are presented in the next Section.

III. Signal Characterisation Results

Using the wing model and testing rig described in Section II, a series of characterisation experiments were carried out in the University of Bristol low turbulence wind tunnel [22]. Quasi-static as well as dynamic tests were performed at air speeds $V = [8, 10, 12, 14, 16, 18, 20]$ m/s to characterise the aerodynamic loads, pressure and strain signals. These tests consisted of α sweeps at various pitch rates. The data collected from these tests was used to identify stall characteristic markers in measured pressure and strain signals, and to acquire data sets for training/validation of an Artificial Neural Network (ANN) estimating airspeed, angle of attack, lift, drag and pitching moment, as well as the characteristic response of the signals to changes in pitch rate (q).

At the beginning of each experiment $\alpha = 0°$ was held, then α was decreased until $\alpha = -15°$ was reached. Then, the direction of the sweep was changed and the motion continues until $\alpha = 20°$ was reached. This cycle was repeated four more times, reaching $\alpha = -15°$ and $\alpha = 20°$, respectively. Lastly, at the end of the fifth cycle ($\alpha = 20°$), the direction of the sweep was changed once more until $\alpha = 0°$ was reached and the experiment ended. During each α sweep, the corresponding q was held constant. α sweeps with $q = [0.1, 0.5, 5, 10, 20, 30, 40, 50]$ °/s were performed. No significant dynamic effects were observed between data sets for $q = [0.1, 0.5, 5]$ °/s, therefore only data corresponding to $q \geq 5$ °/s is considered in the following discussion.

Figure 4 shows the characteristic response signals against α from selected pressure and strain sensors in the distributed sensing array for an experiment with $V = 20$ m/s at various pitch rates. The data in these plots is presented in normalised form. Measured signals were divided by $\frac{1}{2}\rho V^2$ (pressure), $\frac{1}{2}\rho V^2 Sc$ (vertical strain) and $\frac{1}{2}\rho V^2 Sb$ (torsional strain). Figures 4a and 4b show the pressure coefficient variation with α with the plots corresponding to sensor T01 signals for Sections A and B (located at $0.1c$). Section A pressure signal behaves in a parabolic fashion for $-15° \leq \alpha \leq 15°$, with approximate linear behaviour for $-5° \leq \alpha \leq 10°$. Note however that hysteretic behaviour can be observed in this region for $q = 50$ °/s. Section B pressure signal also behaves in a parabolic fashion for $-15° \leq \alpha \leq 15°$, but with a reduced linear behaviour for $0° \leq \alpha \leq 10°$. Hysteretic behaviour can be observed in this region for $q = 50$ °/s. Evidence of flow detachment can be observed for Section B signal at $\alpha > 12°$. Both signals display hysteretic behaviour for the $q = [30$ °/s, 50 °/s$]$ data sets: for Section A this behaviour is seen in $15° \leq \alpha \leq 20°$, while for Section B the region expands to $12° \leq \alpha \leq 20°$.

The vertical bending strain variation with α for sensors SG-A and SG-C is shown in Figures 4c and 4d, respectively. SG-A behaves linearly for $-12° \leq \alpha \leq 10°$, for SG-C the linear region expands to $-15° \leq \alpha \leq 15°$. Hysteretic behaviour is observed for signal SG-A for the $q = [30$ °/s, 50 °/s$]$ data sets in $12° \leq \alpha \leq 20°$. Hysteretic behaviour is also observed for signal SG-C for the $q = 50$ °/s data set in $15° \leq \alpha \leq 20°$.

Figures 4e and 4f show the torsional strain variation with α with the plots corresponding to sensors SG-B and SG-D. Both signals display noisy and highly nonlinear variation with α. However, SG-B shows the characteristic behaviour of aerodynamic pitching moment.

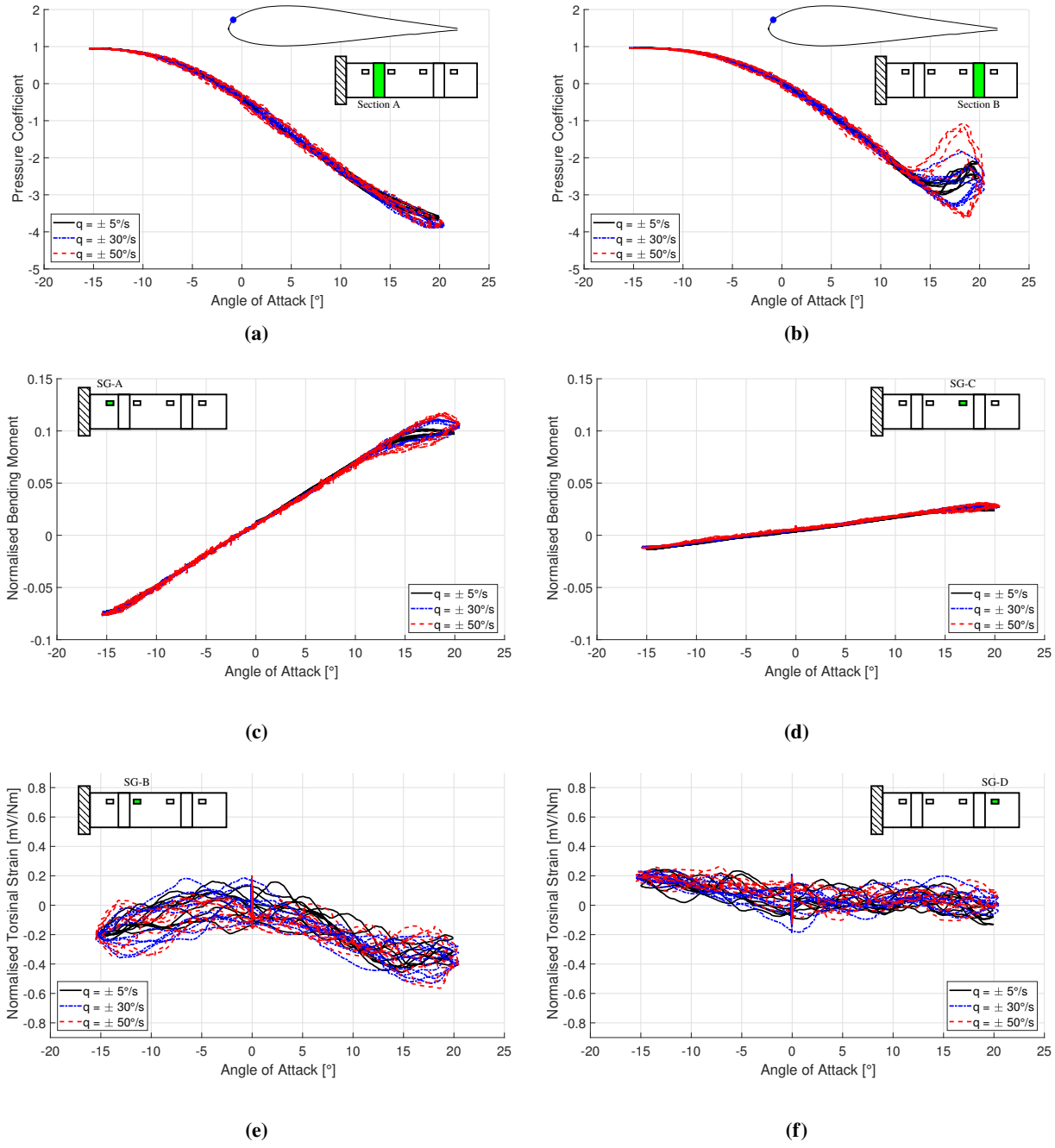

Figure 4 Distributed sensing array signal variation with angle of attack at various pitch rates with $V = 20\,\mathrm{m/s}$: (a) pressure coefficient (sensor T01-A), (b) pressure coefficient (sensor T01-B), (c) normalised bending moment (sensor SG-A), (d) normalised bending moment (sensor SG-C), (e) normalised torsional strain (sensor SG-B) and (f) normalised torsional strain (sensor SG-D).

The results presented in this section show that there is a wealth of information available in the pressure and strain signals. Both types of signals encode the state of the flow around the wing, showing if it is attached, detaching or detached. The signals capture the non-linear behaviour that occurs around stall and at high pitch rates. Both signal

types also show a strong correlation with the normal and tangential force acting on the wing. And lastly, in combination with inertial data (q), the signals capture the hysteretic behaviour of the system offering the potential to take advantage of dynamic lift and related effects. These characteristics can be estimated using the information from the distributed array. In the next section, an example application using the distributed array data to estimate the values of aerodynamic variables and loads is presented.

IV. Aerodynamic variables and loads prediction

A series of feed-forward ANNs were trained to estimate the values of aerodynamic variables and loads using data from the quasi-static and dynamic experiments presented in Section III. To assess the significance of each data set when estimating the aerodynamic variables and loads, a three-level classification of estimators was defined. This classification is based on the available data and the conditions under which the experiments were performed. Figure 5 shows the classification used to define the estimators. The first classification level is defined by the type of training data used for the estimation. There are two sets in this level: quasi-static and dynamic training data. The second classification level is defined by the availability, or not, of inertial data as input, i.e. the measured q is fed, or not, into the estimator. Lastly, the estimators are divided into one of five subsets, depending on the data from the distributed array used as input for estimation: vertical strain (VS), vertical-torsional strain (VAS), pressure (P), pressure-vertical strain (PVS) and pressure-vertical-torsional strain (PAS).

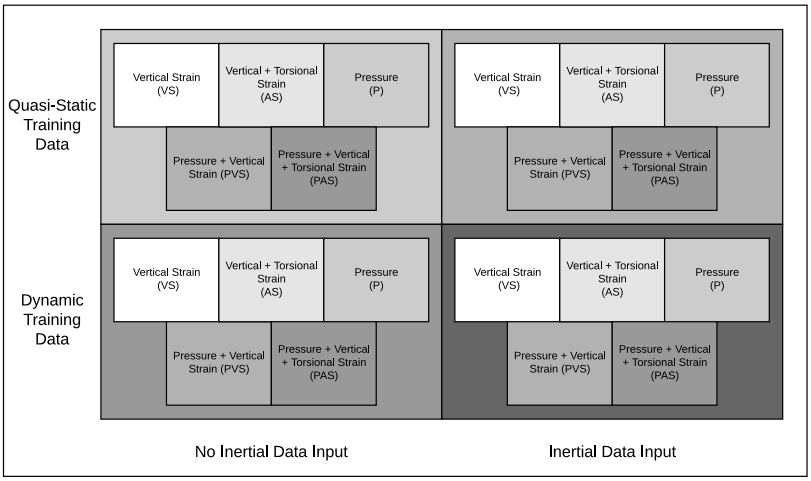

Figure 5 Aerodynamic variables and loads estimators classification.

To assess the performance of each estimator class, the experimental data was divided into three sets: the validation, quasi-static training and dynamic training sets. The validation set consists of data sets for $q = [10, 20, 40]\,^\circ/\mathrm{s}$ and $V = [8, 10, 12, 14, 16, 18, 20]\,\mathrm{m/s}$, as well as data sets with $V = [10, 14, 18]\,\mathrm{m/s}$ and $q = [5, 30, 50]\,^\circ/\mathrm{s}$. The quasi-static training set used data with $V = [8, 12, 16, 20]\,\mathrm{m/s}$ and $q = 5\,^\circ/\mathrm{s}$. Lastly, the dynamic training set used data with $V = [8, 12, 16, 20]\,\mathrm{m/s}$ and $q = [5, 30, 50]^\circ/\mathrm{s}$.

Figure 6 shows the general structure of the ANN used for the estimation of aerodynamic variables and loads. All the trained ANNs consist of three main sections called layers: the input, hidden and output layers. The input layer handles the inputs to the ANN, it conditions the signals to improve the likelihood of successfully training an ANN by scaling them using the mean value and range of the expected inputs. The hidden layer consists of interconnected artificial neurons. For this research, the neurons in the hidden layers used hyperbolic tangent sigmoid functions as activation functions. Lastly, the output layer takes the signals produced by the hidden layer and scales it to match the magnitude of the target function.

For each estimator class, a total of 32 ANNs with different structures were trained to estimate either α, V, D, L or M. A weighted sum of the Mean-Square-Error for training and validation was used as selection criteria to find the ANN that best fitted the data. The ANNs were trained using MATLAB Version 9.2 and Neural Network Toolbox Version 10.0, Release 2017a (The MathWorks, Inc., Natick, Massachusetts, United States), employing the Levenberg-Marquardt back-propagation algorithm as the training function.

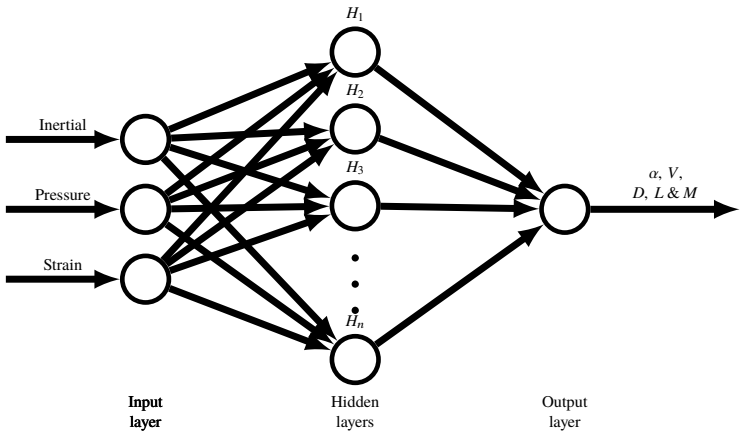

Figure 6 General structure of ANN used for estimation of aerodynamic variables and loads.

Estimation results for α and L are presented next as representative cases. Figure 7 shows the α and L estimation Root-Mean-Square-Error (RMSE) variation between estimator classes for the validation data set. In each plot, the RMSE data is first separated into quasi-static and dynamic training data. A dashed black line separates data without inertial information (cool colours) and data with inertial information (warm colours). Lastly, the amount of data used as input for estimation is indicated by the colour scale, with a dark colour indicating small amount of input data and a lighter colour indicating an increasing amount of input data. Figure 7a shows the overall RMSE variation for α estimation. The first feature that stands out is that VS and AS based estimators perform very poorly within each of the four sub-classes when used to estimate α, with the overall validation RMSE value greater than 2.0°, and when post-stall ($\alpha > 10°$) performance is considered (Figure 7b) the RMSE doubles in value, with the minimum RMSE greater than 4.0°. A second aspect to notice is that the availability of q data does not seem to improve the performance of any of the α estimators significantly, with minimal improvement being seen in any case. Thirdly, when α estimators trained with quasi-static data are compared against the matching estimators trained with dynamic data, there is a significant performance improvement in validation performance. For instance, if VS and AS based estimators are not considered, the RMSE of the remaining estimators in the dynamic class is smaller than 0.2° (Figure 7a), with the post-stall RMSE value approximately increasing to 0.3° (Figure 7b), in comparison, quasi-static trained estimators having RMSE values of approximately 0.3° and 0.5° respectively. Based on the overall estimation RMSE as the selection metric, the IPVS estimator trained with dynamic data is the best estimator for α (Figure 7a).

Figure 7c shows the overall RMSE variation for L estimation. The first feature that stands out is that within each L estimator class, progressive improvement is observed as more input data is used, with P, PVS and PAS based estimators improving in performance as complexity increases (Figure 7c). Secondly, the VS and AS based estimators do not perform as poorly as the ones for α estimation (Figure 7c), but are still the worst performing within each estimator class. Thirdly, the availability of q data does improves the performance marginally, unlike for α. Fourthly, the estimators in the dynamic training data class perform better than those in the quasi-static training data class. For instance, the worst performing estimators in the dynamic class (max. RMSE ≈ 0.95 N) achieve the same performance level as the best performing estimators in the quasi-static class (Figure 7c). The performance trend holds for post-stall conditions ($\alpha > 10°$), with the worst performing estimators RMSE ≈ 1.5 N being similar to the average RMSE of the quasi-static training data class (Figure 7d). Based on the overall estimation RMSE as the selection metric, the IPAS trained with dynamic data is the best L estimator (Figure 7c).

The RMSE performance variation for V, D and M estimators was similar to the reported performance of the α estimators. A comparison between two estimators for both α and L is presented in the following subsections.

A. Angle of attack estimation comparison

Based on the estimation performance presented in Section IV, two α estimators are selected for comparison: the first one (quasi-static P), is the best performing in the quasi-static with no inertial information class and the second one (dynamic IPVS), the best performing in the dynamic with inertial information class. Figure 8 shows the α estimation against the nominal α with $V = 20$ m/s for both quasi-static and dynamic data sets. Figure 8a shows a comparison

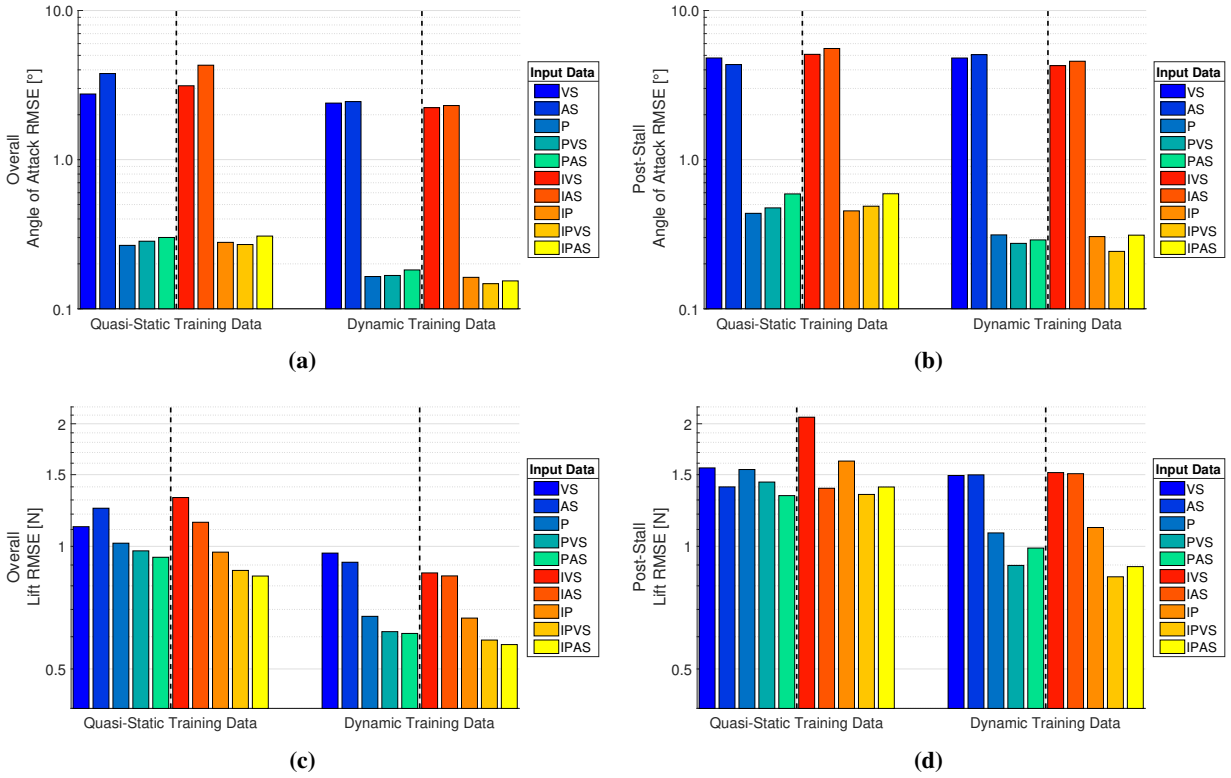

Figure 7 Validation RMSE variation between estimators: (a) angle of attack overall RMSE, (b) angle of attack RMSE for $\alpha > 10°$, (c) lift overall RMSE and (d) lift RMSE for $\alpha > 10°$. (Note logarithmic RMSE axis scale)

between measured and estimated α when quasi-static data is used as input. With the solid black line representing the encoder measurement, the blue dashed line the quasi-static P estimator output and the red dashed-dotted line the dynamic IPVS estimator output. The performance of both the quasi-static P and dynamic IPVS estimators is satisfactory throughout the α range. Both estimators match the encoder measurement well, with the three lines lying one on top of each other. The detailed plot in Figure 8a shows that this trend holds even at high α ($14° \leq \alpha \leq 20°$). Figure 8b shows a comparison between measured and estimated α when dynamic data is used as input. The quasi-static P estimator provides a good α estimate but exhibits hysteretic behaviour throughout the α range, with the hysteretic region increasing for $\alpha \geq 18°$ (detailed plot Figure 8b). The dynamic IPVS estimator is able to correct the hysteretic behaviour effects, even in the $14° \leq \alpha \leq 20°$ region, overlaying the linear signal measured by the encoder. An analysis on the characteristics of the estimation error for the estimation of α and V is presented in Section IV.C.

B. Lift estimation comparison

Based on the estimation performance presented in Section IV, two L estimators are selected for comparison: the first one (quasi-static PAS), is the best performing in the quasi-static with no inertial information class and the second one (dynamic IPAS), the best performing in the dynamic with inertial information class. Figure 9 shows the L estimation against the nominal α with $V = 20\,\mathrm{m/s}$ for both quasi-static and dynamic data sets. Figure 9a shows a comparison between measured and estimated L when quasi-static data is used as input. With the solid black line representing the load cell measurement, the blue dashed line the quasi-static PAS estimator output and the red dashed-dotted line the dynamic IPAS estimator output. Both the quasi-static PAS and dynamic IPAS estimators match the load cell measurement well throughout the α range, with the three lines lying one on top of each other. The detailed plot in Figure 8a shows that the estimation performance remains satisfactory even in the $14° \leq \alpha \leq 20°$ region. Figure 9b shows a comparison between measured and estimated L when dynamic data is used as input. The quasi-static PAS captures the average behaviour of the measured lift signal, but fails to correctly predict the hysteretic behaviour observed throughout the α range. The dynamic IPAS estimator is able to correctly reproduce the hysteretic behaviour throughout the α range, even for in the $10° \leq \alpha \leq 20°$ region. The quasi-static PAS estimator captures the hysteretic behaviour to

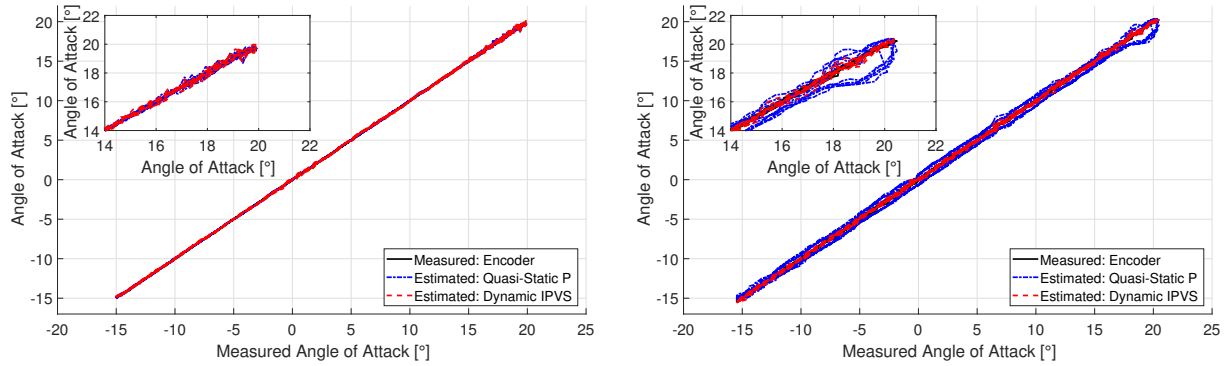

Figure 8 Angle of attack estimation comparison for $V = 20\,\mathrm{m/s}$ at two different pitch rates: (a) $q = \pm 5°$ (quasi-static) and (b) $q = \pm 50°$ (dynamic).

some degree in the $10° \leq \alpha \leq 20°$ region (detailed plot Figure 9b), even though it does not explicitly receive inertial information as input. This suggests that pressure and/or vertical-torsional strain data contain information related to the state of the flow around the wing, with evidence of this observed in the characterisation experiments presented in Section III. Overall this suggests that there is no need to explicitly provide q as input. This is further supported when the validation RMSE for the dynamic PAS and dynamic IPAS estimators are compared, with very similar overall values of approximately 0.6 N and post-stall values of approximately 0.9 N (Figures 7c and 7d). An analysis of the characteristics of the estimation error for the estimation of D, L and M is presented in the following section.

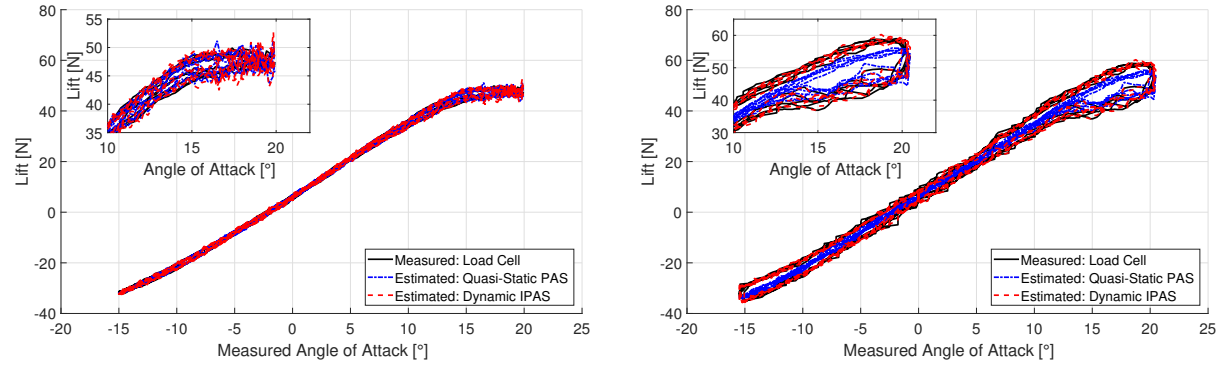

Figure 9 Lift estimation comparison for $V = 20\,\mathrm{m/s}$ at two different pitch rates: (a) $q = \pm 5°$ (quasi-static) and (b) $q = \pm 50°$ (dynamic).

C. Error analysis

Using the best performing estimators, the RMSE was computed for the α, V, D, L and M estimation data, for both the dynamic training and validation sets. The computed RMSE values along with structure characteristics of each ANN are given in Table 2.

Figure 10 shows the error distribution for estimation of the aerodynamic variables distribution. Figure 10a shows the α estimation error distribution for both the training and validation sets. The training error distribution is slightly better than the validation error distribution, with a validation RMSE = 0.15° and for the training set RMSE = 0.11° (Table 2). Figure 10b shows the V estimation error distribution for both the training and validation sets. The training error distribution is slightly better than the validation one, with a RMSE of 0.10 m/s against 0.15 m/s.

Figure 11 the error distribution for estimation of the aerodynamic loads distribution. Figure 11a shows the D estimation error distribution for both the training and validation sets. The training error distribution is very similar

Table 2 Error statistics and characteristics of the best estimators.

Variable	RMSE, Overall		RMSE, $\alpha > 10°$		ANN Characteristics			
	Training	Validation	Training	Validation	Class	# Layers	# Nodes	Structure
α [°]	0.114	0.147	0.205	0.243	Dynamic IPVS	5	22	[7,6,5,3,1]
V [m/s]	0.098	0.148	0.139	0.200	Dynamic P	4	10	[3,3,3,1]
D [N]	0.312	0.332	0.491	0.539	Dynamic IPVS	4	19	[7,6,5,1]
L [N]	0.528	0.574	0.797	0.892	Dynamic IPAS	2	10	[9,1]
M [N m]	0.031	0.030	0.046	0.046	Dynamic PAS	3	11	[7,3,1]

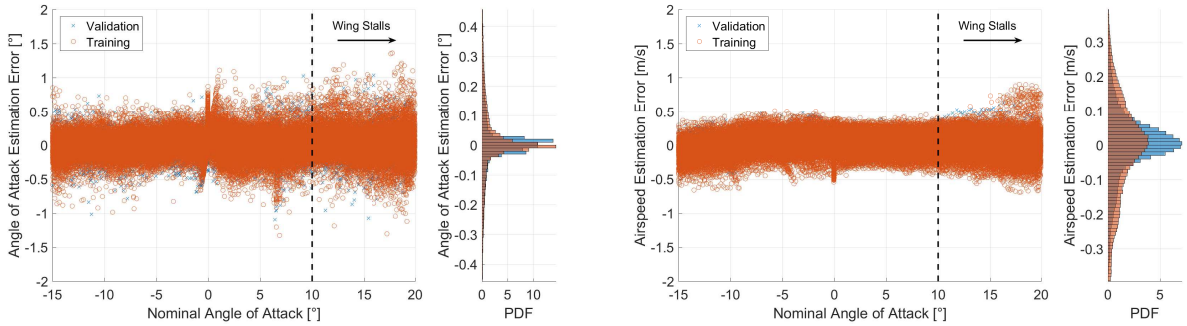

(a) **(b)**

Figure 10 Error distribution for estimation of aerodynamic variables using distributed sensing array: (a) angle of attack and (b) airspeed.

to the validation error distribution, with RMSE for training and validation of 0.31 N and 0.33 N, respectively. For reference D ranges from 6 N to 24 N at 20 m/s. Figure 11b shows the L estimation error distribution for both the training and validation sets. The training error distribution is slightly better than the validation error distribution, with RMSE of 0.53 N for training against 0.57 N for validation. Figure 11c shows the M estimation error distribution for both the training and validation sets. The training error distribution for training and validation are practically the same, with both RMSE for training and validation equal to 0.03 N m. For reference M ranges from -0.4 N m to 0.2 N m at 20 m/s.

V. Concluding Remarks

In this paper, the signal characteristics of a distributed array of sensors measuring the loads (strain) and flow distribution (pressure) acting over the surface of an instrumented wind tunnel wing model were measured. These signals were then used to train various ANNs to estimate the aerodynamic variables and loads, α, V, D, L and M.

Wind tunnel characterisation tests of pressure and strain signals showed that there was a wealth of information available in the pressure and strain signals. This included giving information on the attachment state of the flow and capturing non-linear behaviours such as hysteresis and rate dependent effects. These signals also showed strong correlation with parameters that can not easily be measured in free-flight, such as lift and drag forces. These characteristics can then be estimated using the signals from the distributed array.

In the characterisation results it was observed that the pitching rate q significantly changes the shape and magnitude of both the pressure and strain signals. Based on this behaviour and the available data, estimators were arranged using a three-level classification. It was observed that depending on the class the performance of the estimators improved in the following descending order of importance:

(i) training data; estimators with dynamic training data outperformed the matching estimators trained with quasi-static data,

(ii) availability of inertial data q; availability of inertial information improves performance but only marginally,

(iii) distributed sensing data combination; in general, progressive improvement was observed as the amount of input

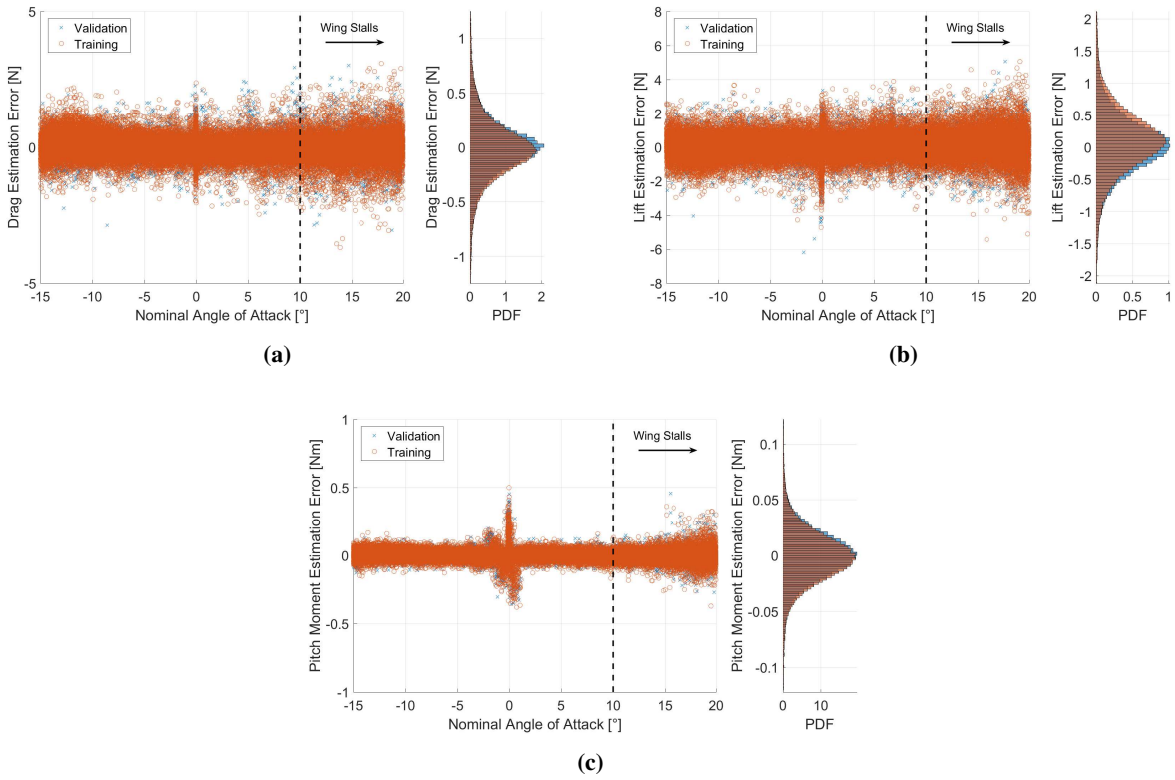

Figure 11 Error distribution for estimation of aerodynamic loads using distributed sensing array: (a) drag, (b) lift and (c) pitching moment.

data increased (PAS/PVS better than P, which in turn is better than VS/AS).

It was observed that all estimators only using combinations of vertical strain and vertical-torsional strain stood out as the worst performing in each estimator class. This is likely to be related in part to airspeed/dynamic pressure information not being explicitly feed into any of the estimators. From characterisation experiments, it was observed that the normalised vertical strain signals are highly correlated to the normal force, behaving in a linear fashion for small α, which suggest that vertical strain could be used to estimate normal force. Another reason for the reduced performance might be the highly nonlinear behaviour of the torsional strain signal with α as well as the signal's poor signal-to-noise ratio.

The best performing ANNs were able to accurately predict α and V even in the stall region, with overall validation RMSE of $0.15°$ and $0.15\,\mathrm{m/s}$ ($0.24°$ and $0.20\,\mathrm{m/s}$ for $\alpha > 10°$), respectively. Similar results have been obtained in wind tunnel experiments with array of sensors mounted on wings in pre-stall conditions [16, 17, 23–26]. It was observed that the α estimator is able to deal with unsteady, nonlinear phenomena, removing hysteretic effects to provide an accurate estimate in high α at high dynamic rates. This suggests that ANN based aerodynamic variable estimators that use pressure and strain data as inputs may be used to provide reliable α and V estimates at high α under dynamic conditions.

Considering estimation of D, L and M, the best performing ANNs were able to achieve overall validation RMSE of $0.33\,\mathrm{N}$, $0.57\,\mathrm{N}$ and $0.03\,\mathrm{N\,m}$, respectively. These provide good estimates even beyond the stall region with RMSE values of $0.54\,\mathrm{N}$, $0.89\,\mathrm{N}$ and $0.05\,\mathrm{N\,m}$ for $\alpha > 10°$. These values are of the same order of magnitude as other research using distributed sensing in wind tunnel experiments [17]. It was observed that the L estimator is able to accurately reconstruct hysteretic behaviour. This suggests that ANN based aerodynamic loads estimators that use pressure and strain data as inputs may be used to exploit dynamic behaviour like dynamic lift to improve the manoeuvrability of UAVs.

These results suggest that pressure and strain sensing could be used in combination with ANN-based estimators to improve flight control performance, by providing accurate estimates of aerodynamic variables and loads. The aerodynamic variables could be fed into model-based controllers, or the aerodynamic loads could be used directly

by physics-based controllers [18, 27, 28]. Alternatively, a more robust estimate of the aircraft's dynamic state can be obtained by fusing the signals from the distributed array with the inertial and visual information of conventional sensors. It has been hypothesised that a similar approach know as "mode sensing" may be used by insects [8]. Another alternative is to use an End-to-End learning approach where systems, typically using convolutional neural networks, are trained to learn direct mappings between control inputs and system outputs [29], resulting in smaller networks with improved performance due to internal components self-optimisation.

In order to develop this approach further there are a number of areas of potential development. A factor that has not been considered so far in the ANN-based estimation is the signal response to control surface deflections. For the system to provide accurate estimates, a model of the signal response to control inputs needs to be included. One way of achieving this would be for an ANN to learn the correlation between control inputs and the expected sensory response and to then filter out the expected sensor response. This ANN would only then provide the signal generated by any external changes. It has been suggested that a similar adaptive filter approach is part of the function of the cerebellum in the mammalian nervous system [30], with other animal groups having equivalent systems involved with their motor control.

Acknowledgments

The authors would like to thank Mr Lee Winter from the University of Bristol wind tunnel laboratory, for his invaluable support and work during the assembly of the pressure ports in the pressure sensing platform used to carry out the experiments presented in this paper.

This project has received funding from the European Research Council (ERC) under the European Union's Horizon 2020 research and innovation programme (grant agreement No 679355).

References

[1] Mohamed, A., Clothier, R., Watkins, S., Sabatini, R., and Abdulrahim, M., "Fixed-wing MAV attitude stability in atmospheric turbulence Part 1: Suitability of conventional sensors," *Progress in Aerospace Sciences*, Vol. 70, 2014, pp. 69–82. DOI: 10.1016/j.paerosci.2014.06.001.

[2] Taylor, G. K., Carruthers, A. C., Hubel, T. Y., and Walker, S. M., "Wing morphing in insects, birds and bats: mechanism and function," *Morphing Aerospace vehicles and structures*, 2012, pp. 11–40.

[3] Watkins, S., Milbank, J., Loxton, B. J., and Melbourne, W. H., "Atmospheric winds and their implications for microair vehicles," *AIAA journal*, Vol. 44, No. 11, 2006, pp. 2591–2600.

[4] Young, J., Walker, S. M., Bomphrey, R. J., Taylor, G. K., and Thomas, A. L., "Details of insect wing design and deformation enhance aerodynamic function and flight efficiency," *Science*, Vol. 325, No. 5947, 2009, pp. 1549–1552.

[5] Muijres, F., Johansson, L. C., Barfield, R., Wolf, M., Spedding, G., and Hedenström, A., "Leading-edge vortex improves lift in slow-flying bats," *Science*, Vol. 319, No. 5867, 2008, pp. 1250–1253.

[6] Shepard, E. L., Williamson, C., and Windsor, S. P., "Fine-scale flight strategies of gulls in urban airflows indicate risk and reward in city living," *Phil. Trans. R. Soc. B*, Vol. 371, No. 1704, 2016, p. 20150394.

[7] Mallon, J. M., Bildstein, K. L., and Katzner, T. E., "In-flight turbulence benefits soaring birds," *The Auk*, Vol. 133, No. 1, 2015, pp. 79–85.

[8] Taylor, G. K., and Krapp, H. G., "Sensory Systems and Flight Stability: What do Insects Measure and Why?" *Insect Mechanics and Control*, Advances in Insect Physiology, Vol. 34, edited by J. Casas and S. Simpson, Academic Press, 2007, pp. 231–316. doi:10.1016/S0065-2806(07)34005-8, URL `http://www.sciencedirect.com/science/article/pii/S0065280607340058`.

[9] Hörster, W., "Histological and electrophysiological investigations on the vibration-sensitive receptors (Herbst corpuscles) in the wing of the pigeon (Columba livia)," *Journal of Comparative Physiology A*, Vol. 166, No. 5, 1990, pp. 663–673.

[10] Brown, R. E., and Fedde, M. R., "Air-flow sensors in the avian wing," *Journal of Experimental Biology*, Vol. 179, 1993, pp. 13–30.

[11] Altshuler, D. L., Bahlman, J. W., Dakin, R., Gaede, A. H., Goller, B., Lentink, D., Segre, P. S., and Skandalis, D. A., "The biophysics of bird flight: functional relationships integrate aerodynamics, morphology, kinematics, muscles, and sensors 1," *Canadian Journal of Zoology*, Vol. 93, No. 12, 2015, pp. 961–975.

[12] Sterbing-D'Angelo, S., Chadha, M., Chiu, C., Falk, B., Xian, W., Barcelo, J., Zook, J. M., and Moss, C. F., "Bat wing sensors support flight control," *Proceedings of the National Academy of Sciences*, Vol. 108, No. 27, 2011, pp. 11291–11296. doi:10.1073/pnas.1018740108, URL http://www.pnas.org/content/108/27/11291.abstract.

[13] Whitmore, S., Cobleigh, B., and Haering, E., Jr, "Design and calibration of the X-33 flush airdata sensing (FADS) system," *36th AIAA aerospace sciences meeting and exhibit*, 1998, p. 201.

[14] Pruett, C., Wolf, H., Heck, M., and SIEMERS III, P., "Innovative air data system for the space shuttle orbiter," *Journal of Spacecraft and Rockets*, Vol. 20, No. 1, 1983, pp. 61–69.

[15] Shen, H., Xu, Y., and Remeikas, C., "Pitch Control of a Micro Air Vehicle with Micropressure Sensors," *Journal of Aircraft*, Vol. 50, No. 1, 2013, pp. 239–248. 10.2514/1.C031894.

[16] Fei, H., Zhu, R., Zhou, Z., and Wang, J., "Aircraft flight parameter detection based on a neural network using multiple hot-film flow speed sensors," *Smart materials and structures*, Vol. 16, No. 4, 2007, p. 1239.

[17] Magar, K. T., Reich, G. W., Kondash, C., Slinker, K., Pankonien, A. M., Baur, J. W., and Smyers, B., "Aerodynamic parameters from distributed heterogeneous CNT hair sensors with a feedforward neural network," *Bioinspiration & biomimetics*, Vol. 11, No. 6, 2016, p. 066006.

[18] Yeo, D., Atkins, E. M., Bernal, L. P., and Shyy, W., "Experimental Validation of an Aerodynamic Sensing Scheme for Post-Stall Aerodynamic Moment Characterization," *AIAA Atmospheric Flight Mechanics (AFM) Conference*, AIAA, Boston, Massachusetts, 2013. DOI: 10.2514/6.2013-4979.

[19] Thompson, R. A., Evers, J., and Stewart, K., "Attitude control augmentation using wing load sensing-A biologically motivated strategy," *Atmospheric Flight Mechanics Conference*, AIAA, Toronto, Canada, 2010. DOI: 10.2514/6.2010-7936.

[20] Castano, L., Airoldi, S., McKenna, T., and Humbert, J. S., "Gust rejection using force adaptive feedback for roll," *14th AIAA Aviation Technology, Integration, and Operations Conference*, AIAA, Atlanta, Georgia, 2014. DOI: 10.2514/6.2014-2588.

[21] Araujo-Estrada, S. A., Salama, F., Greatwood, C. M., Wood, K. T., Richardson, T. S., and Windsor, S. P., "Bio-Inspired Distributed Strain and Airflow Sensing For Small Unmanned Air Vehicle Flight Control," *AIAA Guidance, Navigation, and Control Conference*, 2017, p. 1487.

[22] Barrett, R., "Design and performance of a new low turbulence wind tunnel at Bristol University," *The Aeronautical Journal (1968)*, Vol. 88, No. 873, 1984, p. 86–90. doi:10.1017/S000192400002025X.

[23] Callegari, S., Zagnoni, M., Golfarelli, A., Tartagni, M., Talamelli, A., Proli, P., and Rossetti, A., "Experiments on an aircraft flight parameter detection by on-skin sensors," *Sensors and Actuators A: Physical*, Vol. 130-131, 2006, pp. 155–165. doi:10.1016/j.sna.2005.12.026.

[24] Samy, I., Postlethwaite, I., Gu, D.-W., and Green, J., "Neural-Network-Based Flush Air Data Sensing System Demonstrated on a Mini Air Vehicle," *Journal of Aircraft*, Vol. 47, No. 1, 2010, pp. 18–31. doi:10.2514/1.44157.

[25] Que, R., and Zhu, R., "Aircraft aerodynamic parameter detection using micro hot-film flow sensor array and BP neural network identification," *Sensors (Switzerland)*, 2012. doi:10.3390/s120810920.

[26] Laurence, R. J., Argrow, B. M., and Frew, E. W., "Wind Tunnel Results for a Distributed Flush Airdata System," *Journal of Atmospheric and Oceanic Technology*, Vol. 34, No. 7, 2017, pp. 1519–1528. doi:10.1175/JTECH-D-16-0242.1.

[27] Shen, H., Xu, Y., and Dickinson, B. T., "Micro Air Vehicle's Attitude Control Using Real-Time Pressure and Shear Information," *Journal of Aircraft*, Vol. 51, No. 2, 2014, pp. 661–671. DOI: 10.2514/1.C032375.

[28] Marino, M. J., Watkins, S., Sabatini, R., and Gardi, A., "Sensing Unsteady Pressure on MAV Wings: a New Method for Turbulence Alleviation," *Applied Mechanics and Materials*, Vol. 629, 2006, pp. 48–54. doi:10.4028/www.scientific.net/AMM.629.48.

[29] Bojarski, M., Testa, D. D., Dworakowski, D., Firner, B., Flepp, B., Goyal, P., Jackel, L. D., Monfort, M., Muller, U., Zhang, J., Zhang, X., Zhao, J., and Zieba, K., "End to End Learning for Self-Driving Cars," *CoRR*, Vol. abs/1604.07316, 2016. URL http://arxiv.org/abs/1604.07316.

[30] Dean, P., Porrill, J., Ekerot, C.-F., and Jorntell, H., "The cerebellar microcircuit as an adaptive filter: experimental and computational evidence," *Nature Reviews Neuroscience*, Vol. 11, No. 1, 2010, pp. 30–43.